Astronomy & Astrophysics manuscript no. ngc1835bss
May 9, 2024

The dynamical age of the LMC globular cluster NGC 1835 using the "dynamical clock"⋆

Star density profile and blue straggler stars

Camilla Giusti[1,2], Mario Cadelano[1,2], Francesco R. Ferraro[1,2], Barbara Lanzoni[1,2], Cristina Pallanca[1,2], Enrico Vesperini[3], Emanuele Dalessandro[2], and Maurizio Salaris[3]

[1] Dipartimento di Fisica & Astronomia, Università degli Studi di Bologna, via Gobetti 93/2, I-40129 Bologna, Italy

[2] INAF - Astrophysics and Space Science Observatory Bologna, Via Gobetti 93/3, 40129, Bologna, Italy

[3] Dept. of Astronomy, Indiana University, Bloomington, IN 47401, USA

[4] Astrophysics Research Institute, Liverpool John Moores University, Liverpool L3 5RF, UK

May 9, 2024

ABSTRACT

In the context of the study of the size-age relationship observed in star clusters in the Large Magellanic Cloud and the investigation of its origin, here we present the determination of the structural parameters and the dynamical age of the massive cluster NGC 1835. We have used a powerful combination of optical and near-ultraviolet images acquired with the WFC3 onboard the HST to construct the star density profile from resolved star counts, determining the values of the core, half-mass and tidal radii through the comparison with the King model family. The same data also allowed us to evaluate the dynamical age of the cluster by using the 'dynamical clock'. This is an empirical method that quantifies the level of central segregation of blue stragglers stars (BSSs) within the cluster half-mass radius by means of the A^+_{rh} parameter, which is defined as the area enclosed between the cumulative radial distribution of BSSs and that of a reference (lighter) population. The results confirm that NGC 1835 is a very compact cluster with a core radius of only 0.84 pc. The estimated value of A^+_{rh} (0.30 ± 0.04) is the largest measured so far in the LMC clusters, providing evidence of a highly dynamically evolved stellar system. NGC 1835 nicely fits into the correlation between A^+_{rh} and the central relaxation time and in the anti-correlation between A^+_{rh} and the core radius defined by the Galactic and the Magellanic Cloud clusters investigated to date.

1. Introduction

The Large Magellanic Cloud (LMC) hosts globular clusters (GCs) spanning various ages, ranging from a few million to billions of years (Bica et al. 2008; Nayak et al. 2016). Its star formation history differs significantly from that of the Milky Way (MW), which predominantly hosts very old ($t > 10$ Gyr) GCs. As suggested, e.g., by Fig. 15 of Mackey & Gilmore (2003) and Fig. 1 of Ferraro et al. (2019), during the initial stages of star formation in the LMC (around 13 Gyrs ago), massive clusters ($M > 10^5 M_\odot$) formed at various distances from the galaxy centre. This phase was followed by a period of quiescence, known as the 'age-gap', lasting about 10 billion years. Then, approximately 3 Gyr ago, a period of strong tidal interaction between the MW and the LMC, and/or between the LMC and the Small Magellanic Cloud (SMC) likely began, triggering significant collisions among gas clouds that boosted a second burst of star formation, during which the less massive clusters now observed in the LMC's central regions have been generated (Da Costa 1991; Rich et al. 2001; Bekki et al. 2004; Mazzi et al. 2021).

Unlike the MW, the LMC provides an opportunity to explore the properties of GCs spanning a large range of ages and masses (Elson et al. 1989; Elson 1991; Olszewski et al. 1996; Olsen et al. 1998; Brocato et al. 1996; Mackey & Gilmore 2003; Baumgardt et al. 2013; Ferraro et al. 1995, 2004; Mucciarelli et al. 2006). From these studies, about 30 years ago emerged a peculiar trend between the core radius (r_c) and the chronological (stellar) age of the clusters, the so-called 'size-age conundrum'. Specifically, while young clusters all have small core radii (r_c<2.5 pc), the older ones exhibit a broader range of sizes, reaching up to r_c = 10 pc (Elson et al. 1989; Elson 1991; Mackey & Gilmore 2003). Different solutions to the size-age conundrum have been proposed in the literature, with the most acknowledged one being that presented in Mackey et al. (2008). These authors suggest an evolutionary connection between the younger and older clusters, with the former representing how the latter appeared at the epoch of their formation. Hence, in this framework all clusters were born compact, and subsequent interactions among single stars and binary stellar-mass black holes (BHs) drove core expansion up to the large values of r_c currently observed for the oldest systems.

However, Ferraro et al. (2019) put into evidence a significant difference between the young and the old LMC clusters, and challenged such an evolutionary connection; specifically, Ferraro et al. (2019) pointed out that all the young clusters are significantly less massive than the old ones (see the middle panel in Fig. 1 of Ferraro et al. 2019). Ferraro et al. (2019) proposed instead a new hypothesis to explain the size-age conundrum where the differences in the core radius values among the oldest systems are

⋆ Based on observations with the NASA/ESA HST, obtained under program GO 16361 (PI: Ferraro). The Space Telescope Science Institute is operated by AURA, Inc., under NASA contract NAS5-26555

attributed to variations in their dynamical ages. In fact, GCs are collisional systems, in which the interactions among stars can alter significantly the internal energy budget. Because of these interactions, the heavier stars tend to progressively migrate towards the central regions through the action of dynamical friction, causing a contraction of the core and an increase in the central density until this collapse is halted by the energy provided by interactions with primordial or dynamically formed binary stars (Heggie & Hut 2003). The evolutionary path of a cluster depends both on its internal structure and the tidal field of its host galaxy (see, e.g., Meylan & Heggie 1997). For instance, clusters with higher central density experience a more rapid dynamical evolution than others, due to a larger probability of stellar interactions. Similarly, in clusters located at small galactocentric distances, the stripping action of low-mass stars by the galactic tidal field accelerates the process. This implies that clusters of the same chronological age may be at different stages of their dynamical evolution depending on differences in their initial structural properties and the external environment where they evolved. In particular, in the scenario proposed to explain the observed variety of core radii for the old GCs, loose systems represent dynamically young systems, while the compact ones are the systems in more advanced stages of their dynamical evolution.

Ferraro et al. (2019) demonstrated this hypothesis by measuring the dynamical ages of five old and coeval clusters in the LMC through the 'dynamical clock' method. This approach relies on the properties of a distinct stellar population routinely observed within GCs and known as blue straggler stars (BSSs). The formation processes of these peculiar objects are not yet fully understood, but two main formation scenarios have been proposed so far (see also Bailyn 1995): i) mass-transfer in binary systems (McCrea 1964), and ii) stellar mergers due to direct collisions between two or more stars (Hills & Day 1976). These are both mass-increasing processes, making BSSs more massive (M$\sim 1-1.4 M_{\odot}$, Fiorentino et al. 2014; Raso et al. 2019) than the average of normal stars in old clusters (M$\sim 0.3-0.4 M_{\odot}$). Therefore, under the action of dynamical friction, they sink towards the central region faster than less massive stars. For this reason, they act as excellent gravitational probes and their degree of central segregation compared to that of a normal cluster population can be used as a clock-hand of a 'dynamical chronometer' to measure the dynamical stage of a system (see Ferraro et al. (2012, 2018, 2019, 2020, 2023); Lanzoni et al. (2016). In order to quantify the level of BSS central segregation, Alessandrini et al. (2016) (see also Lanzoni et al. 2016) introduced the A^+_{rh} parameter. It is defined as the area enclosed between the cumulative radial distribution of BSSs and that of a reference population (lighter stars, like main sequence or red giant branch stars) within one half-mass radius (r_h) from the cluster centre. The value of A^+_{rh} provides a measure of the degree of mass segregation of BSS and generally increases during a cluster dynamical evolution (see also Alessandrini et al. (2016) for a discussion of the effects of dark remnants on the evolution of BSS segregation and the A^+_{rh} parameter). This has been demonstrated by the strong correlation between A^+_{rh} and the number of central relaxation times undergone by the system over its lifetime ($N_{\rm relax}$) in a sample of about 50 Galactic GCs (Ferraro et al. 2018, 2023; Beccari et al. 2023). By applying the dynamical clock to five old clusters in the LMC (namely, NGC 1466, NGC 1841, NGC 2210, NGC 2257, Hodge 11), Ferraro et al. (2019) found that they follow the same correlation between N_{relax} and A^+_{rh} drawn by the Milky Way systems, thus demonstrating the validity of the method beyond our Galaxy. Furthermore, this study proved the expected anticorrelation between the core radius and the dynamical age of the five systems, confirming that the wide range of core radii observed for the old LMC clusters is due to their different dynamical stage.

The cluster sample surveyed so far, however, leaves the oldest LMC systems with a very compact core radius still totally unexplored. To fill this gap, here we apply the dynamical clock method to NGC 1835. This cluster is very old (approximately 12.5 Gyr old; Giusti et al. 2024; Olsen et al. 1998) and very compact ($r_c < 0.8$ pc), with a large mass (approximately $6 \times 10^5 M_{\odot}$; Mackey & Gilmore 2003) and a low metallicity ([Fe/H]~ -1.7 dex; Mucciarelli et al. 2021). The present analysis is based on a set of high-resolution Hubble Space Telescope (HST) images acquired with the WFC3 in the cluster direction. These exposures were already used to characterize the properties of a small stellar system named KMK 88-10 located at only 2′ from the cluster, providing evidence that it has been possibly captured by NGC 1835 and it is on the verge of tidal distruption (Giusti et al. 2023). Moreover, in Giusti et al. 2024 we presented the discovery of a very extended blue tail in the horizontal branch (HB) of NGC 1835, and we provided the most precise estimate so far of the cluster age (12.5 ± 1 Gyr), confirming that it is very old. In this paper we determine the star density profile of the cluster to characterise its structural parameters and to investigate its possible core-collapse nature, as indicated in Mackey & Gilmore (2003), and we measure its dynamical age by using the level of BSS segregation, discussing the results in the context of the size-age conundrum.

2. Data analysis

The present study is based on high-resolution images collected with the UVIS channel of the HST/WFC3 in the F300X, F606W, F814W filters, complemented with a simultaneous parallel observations in the F606W and F814W filters acquired with the Wide Field Camera of the Advanced Camera for Surveys (ACS/WFC), under program GO 16361 (PI: Ferraro). The data set and data reduction procedures are described in Giusti et al. (2024). Here we briefly summarize the main points.

The WFC3 has a total field of view of 160″ × 160″, and the cluster centre has been located at the UVIS1 aperture. These data therefore sample the cluster population, both in the optical (F606W and F814W) and in the near-ultraviolet (near UV) band (F300X). The parallel ACS observations sample an LMC field located at ∼ 5′ from the WFC3 pointing, and are therefore used for decontamination purposes. The data reduction procedure was executed with the DAOPHOT II software, following the methodologies delineated in earlier publications (see, e.g. Cadelano et al. 2022a; Onorato et al. 2023; Chen et al. 2023). The only peculiarity is that for the WFC3 data set we followed the so-called 'UV-guided search', which is specifically designed to maximize the detection of hot stars (like extremely-blue HB stars, BSSs, and white dwarfs) in stellar populations where giant stars are dominant (see Paresce et al. 1992; Ferraro et al. 1997, 1998, 1999, 2001, 2003a; Lanzoni et al. 2007; Dalessandro et al. 2013; Raso et al. 2017; Chen et al. 2021, 2022). This approach has led to the discovery of the extended HB blue tail in NGC 1835 (Giusti et al. 2024), which remained undetected in all the previous optical studies of the cluster, and plays a crucial role in the present paper, where the collection of a complete sample of BSSs is required. The approach consists in generating a master list of stars identified in at least half of the near UV (F300X) images, and then force fitting the PSF model to the position of these stars in all the other filters. The magnitude values estimated for each star from different images have been

combined using DAOMATCH and DAOMASTER, and finally calibrated onto the VEGAMAG photometric system by applying the aperture corrections and zero points quoted in the dedicated HST web pages. The instrumental positions have been corrected for geometric distortions (see Bellini et al. 2011 and Meurer et al. 2003 for the WFC3 and the ACS, respectively) and then transformed into absolute coordinates through cross-correlation with the Gaia DR3 catalog (Gaia Collaboration et al. 2022).

The left-hand and central panels of Figure 1 show the near UV and the optical CMDs of NGC 1835, respectively: only stars within the innermost 13″ (corresponding to the cluster half mass radius, see Section 4.1) are plotted to more clearly highlight the cluster population. Being stars with high temperatures ($T_{\rm eff}$ ∼ 7000 K), BSSs are better distinguishable in the near UV plane, where they span a range of about 2.5 magnitudes ($20.5 < m_{\rm F300X} < 23$) above the main sequence turn-off (MS-TO) region. On the other hand, the cold red giant branch (RGB) sequence is better delineated in the optical CMD (at $17.5 < m_{\rm F814W} < 21.5$). For these reasons, the BSS sample and the RGB reference population used in the following analysis (see Section 5) will be selected in the near UV and optical CMDs, respectively. In the right-hand panel we show the CMD of the LMC field region sampled by the ACS parellel observations, in the same filter combination of the cluster optical CMD.

3. Gravitational centre

As already discussed in many works (e.g. Ferraro et al. 1999, 2003b; Lanzoni et al. 2007; Ibata et al. 2009; Miocchi et al. 2013), the precise location of the centre of gravity plays a very important role in the accurate determination of the star density and surface brightness profiles. Mackey & Gilmore (2003) determined the centre position of NGC 1835 from the location of the cluster's surface brightness peak, finding: $\alpha = 05^h : 05^m : 06^s.7$, $\delta = -69° : 24' : 15''$. However, this method is prone to significant biases due to the possible presence of even a few bright stars not located at the cluster's centre, because the surface brightness peak would be systematically shifted towards them. Thanks to our high-resolution dataset, we have been able, instead, to determine the position of the gravitational centre ($C_{\rm grav}$) from resolved star counts using the method outlined in Montegriffo et al. (1995) (see also Lanzoni et al. (2007, 2019)).

This consists of an iterative procedure that starts from a test value of the centre (e.g. a literature value) and determines the average of the coordinates of a sample of stars within a fixed distance r. This procedure produces a new estimate of the centre, from which the next iteration starts. The convergence is fixed when the difference between the position of two successive centres is less than 0.01″. The search radius r must be chosen carefully. It should be larger than the core radius r_c (4.76″ for NGC 1835; Mackey & Gilmore 2003), to work in a region where the stellar density is not uniform. On the other hand, excessively large radii lead to decreased sensitivity to the central concentration. The procedure also allows for a magnitude selection of the sample stars. A faint magnitude limit is necessary to obtain sufficient statistics, but a too high value introduces spurious incompleteness effects. In consideration of these compromises, we iterated the process considering different radius values ($r \leq 10'', 15'', 20''$) and different magnitude limits ($m_{\rm F814W} < 21.5, 22, 22.5$), ensuring in each combination a minimum of 70% completeness (see Sec.6) and thousands of stars included within the search radius. We repeated the iterative procedure for the nine possible combinations. The final value of $C_{\rm grav}$ was then obtained from the average of these nine values: $\alpha = 05^h : 05^m : 6^s.71$, $\delta = -69° : 24' : 14''.78$. Their dispersion provided us with an uncertainty $\sigma = 0.25''$. Our new estimate of $C_{\rm grav}$ is consistent within 1σ with that quoted by Mackey & Gilmore (2003).

4. Star count density profile

We constructed the projected density profile of NGC 1835 from resolved star counts following the procedure described in Miocchi et al. (2013); Lanzoni et al. (2019); Raso et al. (2020). We used only evolved stars ($m_{\rm F300X} < 22.5$), in order to work with objects of approximately the same mass and to ensure a completeness of ∼ 80% in the central region. We also excluded the brightest sources ($m_{\rm F300X} < 18$) to avoid possible biases due to saturation. We divided the WFC3 field of view into 18 radial rings centered on the cluster centre (see Sec. 3) and we divided each ring into four sub-sectors. For each sub-sector, we counted the number of stars in it and we divided the result by the sector's area. We adopted as the density value in each ring the average of the values in the four corresponding sub-sectors, while the error was calculated as their standard deviation. The resulting projected density profile, $\Sigma_*(r)$, is shown in the left panel of Figure 2 (empty circles). The profile shows a central plateau out to ∼ 3″, followed by a gradually decrease in stellar density as the distance from the centre increases. A centrally-flat profile suggests that the cluster is not core-collapsed yet, since a steep power-law cusp in the innermost portion of the density distribution is expected for systems that already experienced this process (see, e.g., Meylan & Heggie 1997). In the outer regions ($r > 40''$), where the LMC field contribution becomes predominant over that of the cluster, a constant density value is observed. From averaging the values of the last 4 bins we derived the LMC mean field density ($\log \Sigma_* \sim -0.9$; see the horizontal dashed line in Fig. 2). We subtracted this quantity from the density value measured in each bin and we then obtained the background decontaminated profile, which is shown as filled circles in the left panel of the figure.

4.1. Fit of the Density Profile

To determine the structural parameters of NGC 1835, we determined the best-fit model to the cluster's background decontaminated density profile by comparing it with the family of spherical, isotropic, single-mass King models (King 1966). The single-mass assumption works with our observed density profile since it was constructed by selecting a sample of stars of approximately the same mass. We followed the procedure outlined in Raso et al. (2020) (see also Pallanca et al. (2023); Deras et al. (2023, 2024)). It consists in a Monte Carlo Markov Chain (MCMC) fitting technique assuming flat priors for the fitting parameters (namely the central density, the concentration parameter c, and the core radius r_c) and a χ^2 likelihood. The resulting best-fit model is represented by the red line in the left panel of Fig. 2.

From this procedure we find that NGC 1835 is a cluster characterized by a relatively high concentration parameter ($c = 1.47^{+0.15}_{-0.14}$, corresponding to a dimensionless central potential $W_0 = 6.8 \pm 0.5$), a very compact core radius $r_c = 3.5^{+0.7}_{-0.5}$ arcsec, a half-mass radius $r_h = 13^{+3}_{-1}$ arcsec, and a tidal radius $r_t = 109^{+36}_{-18}$ arcsec. Knowing the LMC distance (49.6 kpc, Pietrzyński et al. 2019) the results can be expressed as $r_c = 0.84$ pc, $r_h = 3.13$ pc, and $r_t = 26.23$ pc (see Table 1). Mackey & Gilmore (2003) had previously determined some of the structural parameters of the cluster by fitting the observed surface brightness pro-

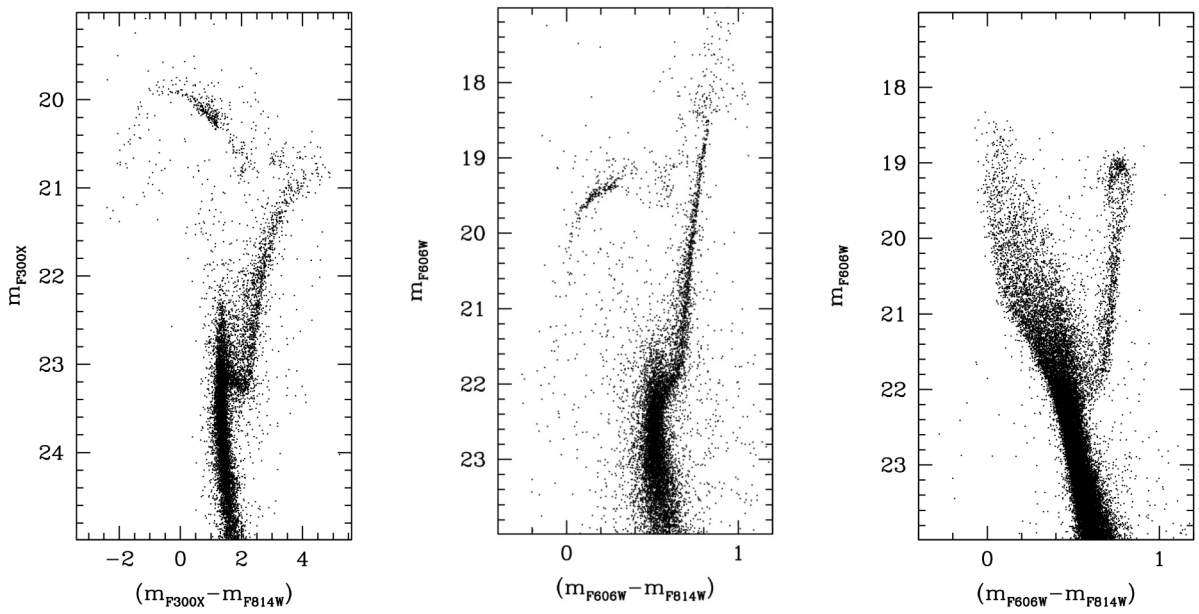

Fig. 1. CMDs of the cluster region and the field region in different filter combinations. *Left panel*: near UV CMD of NGC 1835 for the stars sampled within $r < 13''$ from the centre. *Central panel*: Optical CMD of NGC 1835 for the same stars as in the left panel. *Right panel*: Optical CMD of the LMC field region sampled by the ACS parallel observations.

file with an EFF model (Elson et al. 1987). In particular, they find $r_c = 4.76''$, the small difference with respect to our result being likely attributable to the different adopted approaches. The residuals of the fit (see bottom panel of Fig. 2) show no significant discrepancy from the trend expected from a King model profile in the central regions, further confirming that NGC 1835 is not a core collapse cluster. This is in disagreement with the work of Mackey & Gilmore (2003), where NGC 1835 was classified as a possible core collapse system since a low significance cusp was detected.

4.2. Surface Brightness Profile

To obtain further confirmation of the cluster's structural parameters, we also analyzed the surface brightness profile. The procedure is analogous to the one adopted for the density profile (see Sec. 4). Also in this case, we divided the WFC3 field of view into several concentric rings (21 rings from $C_{\rm grav}$ up to $\sim 120''$) and each ring into four sub-sectors. We adopted as integrated surface brightness of each ring the average of the four values of the corresponding sub-sectors and we assumed the standard deviation as its uncertainty. The resulting surface brightness profile obtained in the $m_{\rm F606W}$ filter is shown in the right panel of Fig. 2 (open circles). The average surface brightness of the last 3 points provided us with the mean surface brightness of the LMC background ($\mu_{\rm F606W} \sim 21.5$ mag arcsec^{-2}). We subtracted this value from all the observed points, obtaining the background decontaminated profile (solid circles). The fit to the profile was carried out following the same procedure described above, comparing it with the family of King models. The results have provided a King concentration index $c = 1.57 \pm 0.02$, a central surface brightness $\mu_{\rm F606W,0} = 15.6$ mag arcsec^{-2}, a core radius $r_c = 3.45^{+0.06}_{-0.04}$ arcsec (0.83 pc), an half-mass radius $r_h = 15^{+0.2}_{-0.3}$ arcsec (3.61 pc), and a tidal radius $r_t = 137 \pm 3$ arcsec (32.72 pc). All these quantities are in good agreement within the errors with the results obtained from the fit of the star count density profile. Even in this case, no evidence of central cusp is found.

5. Measuring the dynamical age

This work is mainly devoted to determine the dynamical age of NGC 1835 through the dynamical clock, which measures the level of central sedimentation of BSSs with respect to a lighter reference population, using the A^+_{rh} parameter (Alessandrini et al. 2016). Hence, after estimating the central relaxation time through the standard approximated approach described in Djorgovski (1993), in this section we discuss the necessary preliminary steps and the final determination of A^+_{rh}.

5.1. The central relaxation time

Under the assumption of a spherically symmetric and isotropic stellar system well reproduced by a King model, we computed the central relaxation time (t_{rc}) of the cluster following equation (10) in Djorgovski (1993, see also Spitzer 1987):

$$t_{rc} = 1.491 \times 10^7 \times \frac{k}{\ln(0.4N_*)m_*}\rho_{M,0}^{1/2} r_c^3, \quad (1)$$

where the constant $k \sim 0.5592$, $N_* = M_{cl}/m_*$ is the number of stars in the cluster of mass M_{cl}, $m_* = 0.3M_\odot$ is the average stellar mass, $\rho_{M,0}$ is the central mass density in units of $M_\odot$ pc^{-3}, r_c is the core radius in parsecs, and t_{rc} is expressed in years. We adopted the cluster total mass provided in (Mackey & Gilmore 2003) ($\log M/M_\odot = 5.83$ that was estimated by using a mass-to-light ratio $M/L_V = 3.56$) rescaled to $M/L_V = 2$, which is the typical value for 10-13 Gyr old clusters (Maraston 1998). In addition, to keep the work consistent with the assumptions of Ferraro et al. (2019), we measured $\rho_{M,0}$ from the equations (4), (5), (6) of Djorgovski (1993), adopting the concentration parameter c and the core radius r_c determined from the star density profile fit (see Table 1), and the central surface brightness $\mu_{555}(0) = 16.37$ quoted in Mackey & Gilmore (2003). The result for NGC 1835 is $\log(t_{rc}/{\rm yr}) = 8.16$.

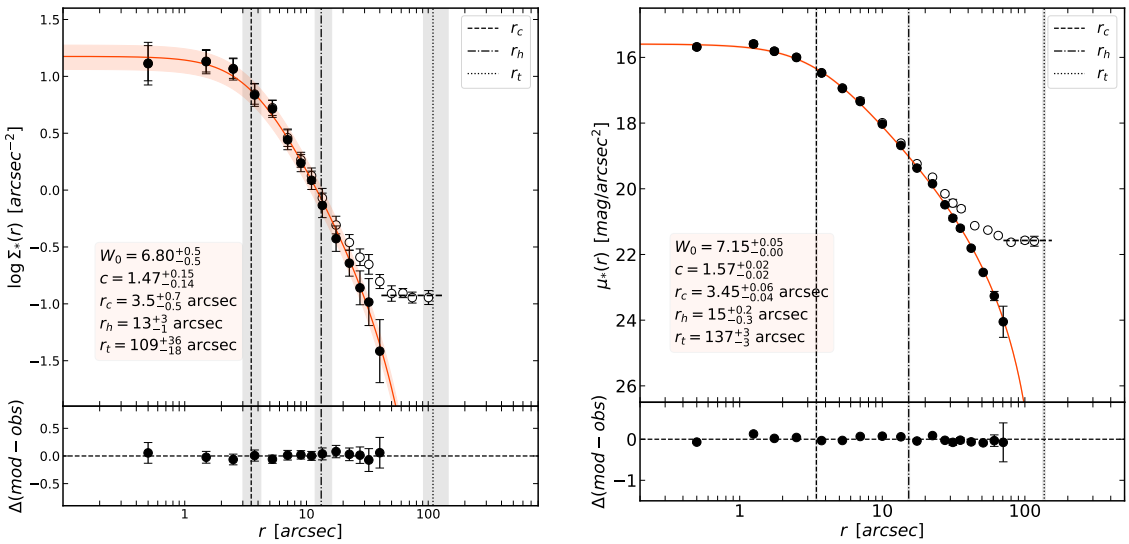

Fig. 2. Density and brightness profiles of NGC 1835. *Left panel*: Projected density profile of NGC 1835 obtained from star counts in concentric annuli around the cluster centre (empty circles). The horizontal dashed line marks the LMC field density that has been subtracted to the observed points to determine the background subtracted profile (filled circles). The red solid line represents the best-fit King model to the cluster density profile and the red stripe outlines the range of $\pm 1\sigma$ solutions. The vertical lines mark the locations of the core radius (dashed line), half-mass radius (dot-dashed line), and tidal radius (dotted line), with their respective 1σ uncertainties indicated by gray stripes. The values of the main structural parameters determined from the fitting process are also marked (see details in the text). *Right panel*: Same as in the left panel, but for the surface brightness profile of NGC 1835 in the F606W filter.

We used this value to obtain a first indication about the dynamical status of the cluster through the parameter $N_{\rm relax}$. This is defined as the ratio between the system's chronological age and its current central relaxation time, thus quantifying the number of t_{rc} experienced by the system during its lifetime. A high value of $N_{\rm relax}$ identifies dynamically evolved clusters, whereas a low value corresponds to dynamically young systems. For NGC 1835, using the chronological age by Giusti et al. (2024) (12.5 Gyr) we find $N_{\rm relax}$ = 86.9. This is one of the largest value obtained so far in the LMC (see Ferraro et al. (2023)), meaning that NGC 1835 is highly dynamically evolved.

Parameter	Estimated value
Centre of gravity	$\alpha_{J2000} = 05^h05^m06^s.7$
	$\delta_{J2000} = -69°24'15''$
Age	$t = 12.5 \pm 1$ Gyr
King concentration	$c = 1.47^{+0.15}_{-0.14}$
Central dimensionless potential	$W_0 = 6.8^{+0.5}_{-0.5}$
Core radius	$r_c = 3.5^{+0.7}_{-0.5}$ arcsec (0.84 pc)
Half mass radius	$r_h = 13^{+3}_{-1}$ arcsec (3.13 pc)
Tidal radius	$r_t = 109^{+36}_{-18}$ arcsec (26.23 pc)
Central relaxation time	$\log t_{rc} = 8.158$ (yr)
Age/Central relaxation time	$N_{\rm relax} = 86.9$

Table 1. Summary of the main properties of NGC 1835 estimated in this work from the fit of the star counts density profile (see left panel of Fig.2). The age was estimated in Giusti et al. (2024).

5.2. Selection of BSSs and reference population

The first step for estimating the A^+_{rh} parameter of NGC 1835 is to select its population of BSSs and reference stars. In a cluster's CMD, BSSs are found in the region bluer and brighter than the cluster MS-TO. We followed the selection procedure already described in several works (see Ferraro et al. 1992, 2001, 2003a, 2023.

Due to effective temperatures larger than those of MS and RGB stars, BSSs are best selected in CMDs built with blue and possibly UV filters. We therefore drew the BSS selection box in the ($m_{\rm F300X}$, $m_{\rm F300X}$-$m_{\rm F814W}$) UV plane: see the multi-sided polygon shown in the left panel of Figure 3. We constructed the left side of the polygon by adopting as an approximate reference the cluster zero-age MS (ZAMS), represented in the figure by a PARSEC (Marigo et al. 2017) isochrone with a very young age (40 Myr, red dotted line). The top and right-hand sides are designed to exclude the bulk of HB and RGB stars. In general, the location of the bottom side of the box is somehow arbitrary, as there is no clear division between the MS-TO and BSSs. Usually, it is assumed that the BSS population begins 4-5 σ magnitudes above the MS-TO, where σ is the photometric error at this magnitude level. However, both to minimize the risk of contamination from MS-TO stars and blends, and to increase the efficiency of the A^+_{rh} parameter, Ferraro et al. (2018) selected only the brightest portion of the BSS sequence, where the most massive BSSs are expected to be located. Thus, they considered only BSSs that are approximately $0.2M_\odot$ more massive than MS-TO stars. To construct the stellar evolutionary tracks in the F300X, we downloaded PARSEC isochrones[1] (Marigo et al. 2017) in this filter in a very wide age range (500 Myr-21 Gyr) in steps of 10 Myr and with properties compatible with those of NGC 1835: metallicity [Fe/H]= −1.7 and α−element abundance [α/Fe]= +0.4 Mucciarelli et al. (2021), and standard helium abundance (Y = 0.248). The track corresponding to the $0.8M_\odot$ stars (rightmost solid line in Fig. 3) well reproduces, as expected, the MS-TO region. Hence, we adopted as threshold for the bright BSS sample the position of the $1M_\odot$ evolutionary track (leftmost solid line in Fig. 3). The final BSS sample is shown by the blue circles in the figure, and it contains 86 objects.

[1] http://stev.oapd.inaf.it/cgi-bin/cmd

Since the MS-TO region is contaminated from LMC field stars, we chose the RGB stars as reference population. We selected them in the optical CMD (where they appear more evident and brighter than hot populations) and in a magnitude range similar to that covered by the BSS sample in this plane (see the black box in the right panel of Fig. 3). This avoids both faint magnitudes, to prevent incompleteness problems, and bright magnitudes, to prevent saturation effects. We obtained a very rich final sample of 596 objects. Given the large statistics of this sample, small differences in the selection lead to negligible differences in the value of A^+_{rh} (see below).

5.3. The A^+_{rh} parameter

As mentioned in Sec.1, the A^+_{rh} parameter is defined as the area enclosed between the normalized cumulative radial distribution of BSSs and that of a reference population of lighter stars, counted within one half-mass radius from the cluster centre. To obtain a meaningful value of A^+_{rh}, it is therefore crucial to assess the level of photometric completeness and of field contamination of both population.

To estimate the completeness information, we carried out artificial star experiments using the prescriptions discussed in Dalessandro et al. (2015); Cadelano et al. (2020). We determined the mean ridge lines of the BSS sequence (down to $m_{\rm F300X} \sim 23$) and of the RGB+MS population (between $m_{\rm F814W} \sim 17.8$ and $m_{\rm F814W} \sim 26$) in the ($m_{\rm F606W}, m_{\rm F300X} - m_{\rm F606W}$) and ($m_{\rm F606W}, m_{\rm F606W} - m_{\rm F814W}$) CMDs, respectively. We then generated a list of artificial stars with an input $m_{\rm F606W}$ magnitude within the considered range, and assigned to each star the corresponding ($m_{\rm F300X} - m_{\rm F606W}$) or ($m_{\rm F606W} - m_{\rm F814W}$) colour according to the respective mean ridge line. These artificial stars have then been added to the acquired images using the DAOPHOT/ADDSTAR software. They have been positioned in a grid of cells with side corresponding to ten times the typical FWHM of the point spread function (PSF) and, in order to avoid artificial crowding effects, only one star at a time was simulated in each cell. Using the PSF model already derived, we repeated the data reduction process in the multiple modified images, and we obtained a catalogue of ~ 454000 and ~ 208100 stars for the BSS and the MS+RGB populations, respectively. We simulated the stars only for the WFC3 UVIS1 detector. This choice is dictated by the fact that the A^+_{rh} parameter is determined from the stars located within one half-mass radius, which is just 13″ for NGC 1835 (see Sec. 4). The completeness C is defined as the ratio between the number of stars recovered in output at the end of the artificial star test (N_o), and the number of input stars actually simulated (N_i). The completeness curves for the three radial bins ($r/r_h \leq 1/3$, $1/3 < r/r_h \leq 2/3$, $2/3 < r/r_h \leq 1$) that will be used in the calculation of A^+_{rh} (see Sec. 5) are shown in Figure 4. The left panel shows the completeness curves as a function of the $m_{\rm F300X}$ magnitude in the three radial bins for the simulated BSSs, while the right panel shows C versus $m_{\rm F814W}$ for the simulated MS+RGB population. These results guarantee that the selected BSS and RGB populations, which extend down to $m_{\rm F300X} \sim 22$ and $m_{\rm F814W} \sim 20.2$ respectively, are poorly affected by incompleteness, both showing C> 80%. Nevertheless, we corrected the two samples by using the derived completeness curves: to build the cumulative radial distributions, each star has been counted as 1/C (instead of 1), with the value of C being derived from the incompleteness curves based on the star magnitude and cluster-centric distance. Thus the completeness-corrected total numbers of BSSs and RGB stars amount to 93.9 and 623.6 stars, respectively, with a correction of the observed sample of only a few percent (9% and 5% respectively).

To correct for LMC field contamination, we took advantage of the parallel ACS observations. Indeed, the CMD plotted in the rightmost panel of Fig. 1 shows that both the BSS and the RGB regions suffer from a non negligible contamination from field stars, as expected in the case of a GC located near the central bar of the LMC. The decontamination via proper motions is not possible. In fact, just another HST dataset centered on NGC 1835 is available in the archive, but it has been acquired with the WFPC2 in 1995 (Olsen et al. 1998), while higher quality observations and a longer time baseline would be necessary, given the distance of the LMC and the similar motion of the GC and the host galaxy. For this reason, we decided to perform a statistical decontamination exploiting the parallel ACS pointing (e.g. Dalessandro et al. 2019). First of all, since for this dataset only the F606W and F814W filters are available, we transported the BSS selection box (previously defined in the near UV CMD; see Fig. 3) in the optical ($m_{\rm F814W}, m_{\rm F606W}$-$m_{\rm F814W}$) plane. This is shown in panel (a) of Figure 5, where the blue circles are the BSSs selected in the near UV, and the box has been drawn to enclose them. Panel (b) shows the same box superposed to the ACS sample. The selection box of RGB stars was already defined in the optical plane, and it is shown superposed to the cluster WFC3 and the field ACS CMDs in panels (c) and (d) of Fig. 5, respectively. We counted the number of field stars falling in the two boxes and we divided the values by the area sampled by the ACS/WFC observations, obtaining the number density of field stars populating the CMD regions covered by the two boxes: $\rho_{\rm field,BSS} = 0.0562 \pm 0.0012$ arcsec^{-2}, $\rho_{\rm field,RGB} = 0.0092 \pm 0.0005$ arcsec^{-2}. Thus, we expect that within one half-mass radius ($r_h = 13''$), a total of 30 LMC stars contaminate the BSS sample, and 5 contaminate the RGB sample. However, the different radial distribution of field stars with respect to that of cluster stars must be taken into account for a proper field decontamination procedure. In fact, while the distribution of the LMC field is essentially uniform over the cluster size scale, the radial distributions of cluster BSSs and RGB stars follow the King profile (see Fig. 2), with a sensibly increasing star density toward the centre of the system. Thus, we divided the field of view included within r_h in the same three concentric radial annuli adopted above: $r/r_h \leq 1/3$, $1/3 < r/r_h \leq 2/3$, and $2/3 < r/r_h \leq 1$. Then, by multiplying the estimated star density by the area of each radial bin ($A_{\rm bin}$), we determined the number of contaminating field stars expected in the bin: $N_{\rm field,pop}(r) = \rho_{\rm field,pop} \times A_{\rm bin}$ (with pop=BSS, RGB). The resulting values are listed in Table 2.

To build the cumulative radial distributions, we randomly subtracted these numbers of stars from the completeness-corrected samples of BSSs and RGB stars, and we obtained the value of A^+_{rh} as the area of the region bounded by the two cumulative functions. We repeated the measurement of A^+_{rh} 100 times, each time randomly removing from the samples a number of stars equal to $N_{\rm field,pop}(r)$ in each bin. We then adopted as final estimate of the parameter the average of the 100 values of A^+_{rh} computed in this way, finding $< A^+_{rh} >= 0.30$. Once the photometric incompleteness and field contamination are taken into account, the main uncertainty affecting the result is due to the limited statistics of the BSS sample. We therefore evaluated it by using a jackknife bootstrapping technique (see Lupton 1993). Given a sample of N BSSs, it consists in repeating the calculation of A^+_{rh} for N times, each time removing one different star. The final uncertainty is therefore calculated as $\sigma_{A^+_{rh}} = \sigma_{\rm distr} \times \sqrt{(N-1)}$, where $\sigma_{\rm distr}$ is the standard deviation of the N estimates of the

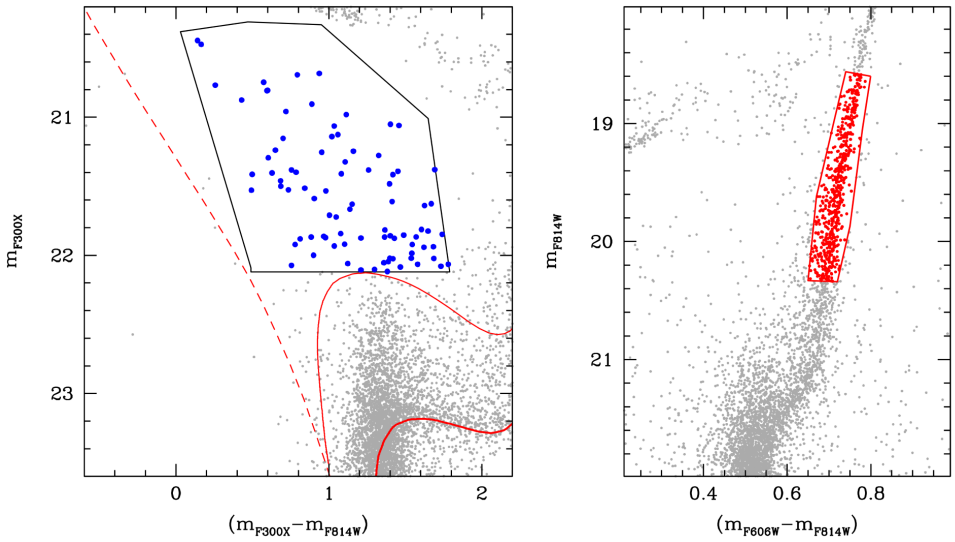

Fig. 3. BSS and RGB samples selection. *Left panel*: near UV CMD of NGC 1835 with the selected BSS sample shown with blue circles. The rightmost solid line is the evolutionary track corresponding to a mass $0.8 M_{\odot}$. The leftmost solid line is the evolutionary track of a $1 M_{\odot}$ mass. The dotted line is the PARSEC isochrone corresponding to a very young age (40 Myr), representing the cluster ZAMS. *Right panel*: Optical CMD of NGC 1835 with the selected RGB sample shown with red circles.

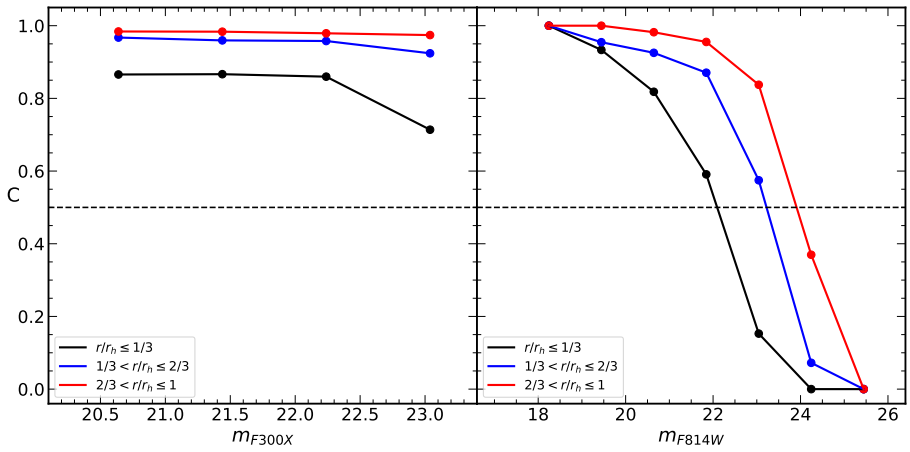

Fig. 4. Completeness curves of the BSS and MS+RGB populations as a function of the $m_{\rm F300X}$ and the $m_{\rm F814W}$ magnitudes (left and right panels), respectively. The different line colours refer to three different radial distances from the cluster centre (see labels).

	N_{TOT}	$N(r/r_h < 1/3)$	$N(1/3 < r/r_h < 2/3)$	$N(2/3 < r/r_h < 1)$
BSS	93.9 (30)	48.6(3)	25(10)	20.3(17)
RGB	623.6 (5)	165.6(1)	280.2(1)	177.8(3)

Table 2. Completeness-corrected samples of BSSs and RGB stars (top and bottom row, respectively), and number of estimated field contaminants (values enclosed in the brackets). N_{TOT} is the total number of stars, while the last three columns provide the numbers of stars estimated in the three adopted radial bins.

A^+_{rh}. We found $\sigma_{A+} = \pm 0.04$. One of the random realizations of the cumulative radial distributions of BSSs (blue curve) and RGB stars (in red) is shown in Figure 6, where the grey-shaded area represents the A^+_{rh} parameter.

6. Discussion and Conclusions

The result obtained for NGC 1835 can now be compared with the outcomes of previous works. Indeed, similar studies were conducted for a total of 52 Galactic GCs (48 systems in Ferraro et al. 2018, NGC 6256 in Cadelano et al. 2022b, and 3 other clusters in Ferraro et al. 2023), plus a total of 7 clusters in the Magellanic Clouds (5 old systems in the LMC and two young ones in the SMC; see Ferraro et al. 2019 and Dresbach et al. 2022, respectively). The left panel of Figure 7 shows the trend between $N_{\rm relax}$ (the number of central relaxation times suffered by each system) and the value of A^+_{rh} for all the clusters consistently investigated in previous studies and for NGC 1835 (shown in red). The new

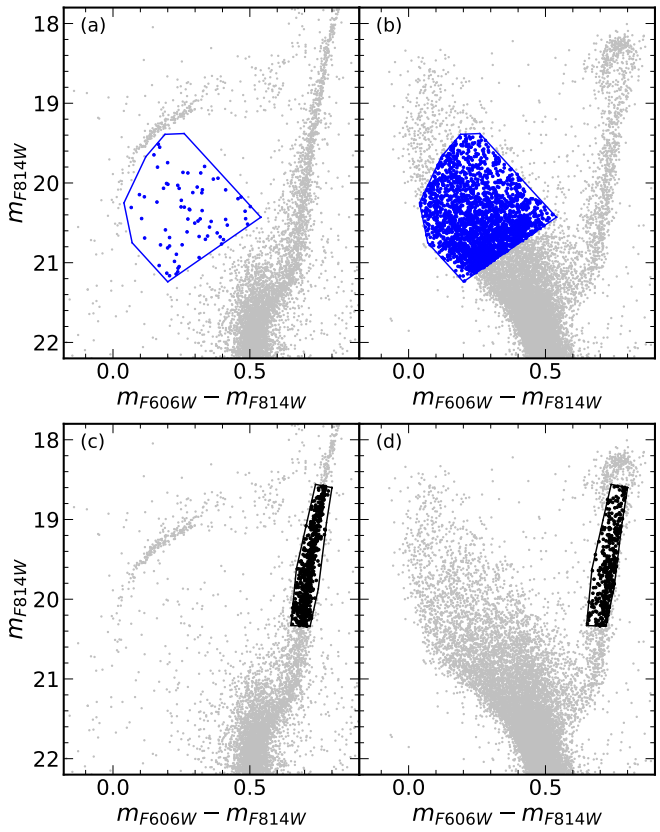

Fig. 5. Decontamination process for the BSS and RGB samples. *Panel (a)*: Optical CMD for the stars sampled by the WFC3 observations within one half-mass radius from the cluster centre (grey dots). The blue circles mark the position of the BSSs selected by using the near UV box drawn in Fig. 3, and the blue countour enclosing these objects is the adopted BSS selection box in the optical CMD. *Panel (b)*: Optical CMD of the stars sampled by the ACS parallel observations (grey dots). The blue contour is the optical selection box defined in panel (a), and the blue circles marks all the stars included within it. *Panel (c)*: Optical CMD for the WFC3 stars sampled within one half-mass radius from the cluster centre (grey dots). The RGB selection is marked in black. *Panel (d)*: Optical CMD of the ACS stars sampled (grey dots), with the same selection box marked in panel (c). The black circles highlight the stars included within it.

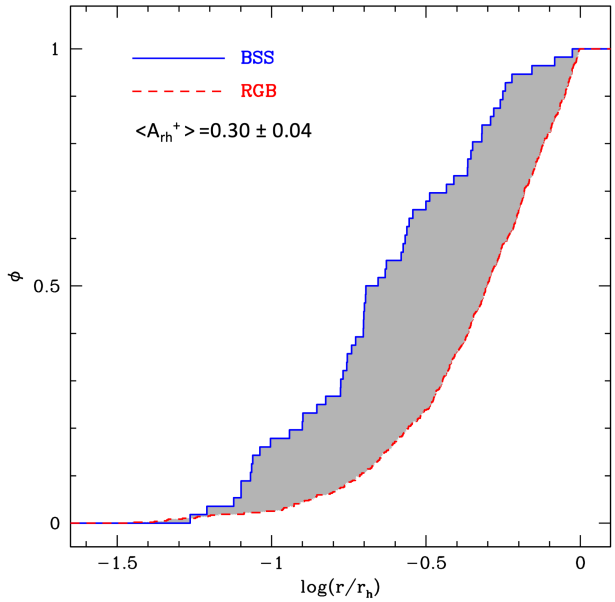

Fig. 6. Normalized cumulative radial distributions of BSSs (blue solid line) and RGB stars (red dashed line) in one of the random realizations used to estimate the A^+_{rh} parameter in NGC 1835. The area enclosed between the two curves corresponds to the value of A^+_{rh} (see label).

determination well fits into, and therefore further reinforce, the close correlation observed between the two parameters.

It is interesting to point out that the MW, the LMC and the SMC clusters all fall along the same relationship, indicating that the dynamical clock parameter can provide a measure of cluster's dynamical ages also outside the MW. As previously discussed, the existence of such a strong correlation between A^+_{rh} and N_{relax} clearly shows that they both trace the dynamical aging of star clusters. However, Ferraro et al. 2023 pointed out that A^+_{rh} provides a better measure of the dynamical history and dynamical age of a cluster than N_{relax}. As discussed in Ferraro et al. (2023), t_{rc} is a parameter determined by the present-day dynamical properties of star clusters, which can be the result of quite different combinations of initial conditions and evolutionary paths. Hence, t_{rc} is not necessarily representative of a specific and unique dynamical history of each stellar system. Conversely, the current level of BSS central concentration is the direct outcome of the many internal and external phenomena that, during the entire cluster lifetime, have modified and characterized the mass segregation process. Thus, the main advantages of the A^+_{rh} parameter with respect to t_{rc} can be summarized as follows: (1) the A^+_{rh} parameter is entirely and directly measured from observations; (2) it is specifically designed to have maximum sensitivity in quantifying the mass segregation of the heaviest and brightest (hence, easily identifiable) stellar population (the BSSs); (3) at odds with t_{rc}, its definition does not require over-simplying assumptions (e.g. spherical symmetry, no rotation, King model structure) or approximations (for instance the definition of r_c, which is very uncertain, in particular, in dynamically evolved stellar system where the presence of a central cusp makes the definition more complicated and possibly meaningless).

In addition, the value of A^+_{rh} seems to be a very promising discriminator between non core-collapsed and core-collapsed clusters. In fact, Ferraro et al. (2023) have shown that 7 Galactic GCs with measured A^+_{rh} and classified as post core-collapsed clusters from the evidence of a central cusp in their density profile all exhibit $A^+_{rh} > 0.29$. In this respect, NGC 1835 (for which we estimate $A^+_{rh} = 0.30 \pm 0.04$) likely is on the verge to core collapse.

The right panel of Fig. 7 shows the relationship between A^+_{rh} and the core radius for the same systems. As already discussed in Ferraro et al. (2019), it shows that clusters with a larger core radius correspond to dynamically younger systems characterized by low degrees of spatial segregation of their most massive visible stars (corresponding to lower A^+_{rh} values) while those with a smaller core radius are in more advanced dynamical stages with a stronger degree of mass segregation. NGC 1835 nicely falls along this anticorrelation, showing the highest value of A^+_{rh} in the LMC (hence, the most advanced dynamical age), consistent with its very small core radius value. So, while Mackey et al. (2008) proposed to resolve the size-age conundrum by advocating the action of binary BHs that progressively drive core expansion of the systems, the range of clusters core radii may simply be a consequence of differences in the clusters dynamical ages. Furthermore, as discussed by Ferraro et al. (2019), young and old clusters exhibit very different properties in terms of mass (where the older clusters are more massive than the younger ones) and

distance from the LMC centre, thus excluding the existence of a simple and direct evolutionary sequence linking the two groups of clusters.

Finally we point out that the young clusters in the LMC are low-mass systems with small core radii and located in the most central regions of the galaxy (see the middle and bottom panels in Fig.1 of Ferraro et al. (2019)). The lack of young clusters with large core radii may be due to the early disruption of these clusters; as proposed by Ferraro et al. (2019), it is plausible that, in this low-mass regime, only the most compact clusters managed to endure the tidal forces exerted by the host galaxy and survived to the present days, while the low mass/low-concentration systems have been disrupted.

In conclusion, the study of the structure of NGC 1835 and the degree of segregation of its BSS presented in this paper further extended previous investigations by adding information about a dynamically old cluster characterized by a significant BSS spatial segregation and bridging the gap between the dynamical characterization of clusters in the Milky Way and the Magellanic Clouds.

Acknowledgements. This work is part of the project Cosmic-Lab at the Physics and Astronomy Department "A. Righi" of the Bologna University (http://www.cosmic-lab.eu/ Cosmic-Lab/Home.html).

References

Alessandrini, E., Lanzoni, B., Ferraro, F. R., et al. 2016, ApJ, 833, 252. doi:10.3847/1538-4357/833/2/252
Bekki, K., Couch, W. J., Beasley, M. A., et al. 2004, ApJ, 610, L93. doi:10.1086/423372
Bellini, A., Anderson, J., & Bedin, L. R. 2011, PASP, 123, 622. doi:10.1086/659878
Bica, E., Bonatto, C., Dutra, C. M., et al. 2008, MNRAS, 389, 678. doi:10.1111/j.1365-2966.2008.13612.x
Baumgardt, H., Parmentier, G., Anders, P., et al. 2013, MNRAS, 430, 676. doi:10.1093/mnras/sts667
Bailyn, C. D. 1995, ARA&A, 33, 133. doi:10.1146/annurev.aa.33.090195.001025
Beccari, G., Cadelano, M., & Dalessandro, E. 2023, A&A, 670, A11. doi:10.1051/0004-6361/202244288
Brocato, E., Castellani, V., Ferraro, F. R., et al. 1996, MNRAS, 282, 614. doi:10.1093/mnras/282.2.614
Cadelano, M., Dalessandro, E., Webb, J. J., et al. 2020, MNRAS, 499, 2390. doi:10.1093/mnras/staa2759
Cadelano, M., Dalessandro, E., Salaris, M., et al. 2022, ApJ, 924, L2. doi:10.3847/2041-8213/ac424a
Cadelano, M., Ferraro, F. R., Dalessandro, E., et al. 2022, ApJ, 941, 69. doi:10.3847/1538-4357/aca016
Chen, J., Ferraro, F. R., Cadelano, M., et al. 2021, Nature Astronomy, 5, 1170. doi:10.1038/s41550-021-01445-6
Chen, J., Ferraro, F. R., Cadelano, M., et al. 2022, ApJ, 934, 93. doi:10.3847/1538-4357/ac7a45
Chen, J., Ferraro, F. R., Salaris, M., et al. 2023, ApJ, 950, 155. doi:10.3847/1538-4357/acd173
Da Costa, G. S. 1991, The Magellanic Clouds, 148, 183
Dalessandro, E., Salaris, M., Ferraro, F. R., et al. 2013, MNRAS, 430, 459. doi:10.1093/mnras/sts644
Dalessandro, E., Ferraro, F. R., Massari, D., et al. 2015, ApJ, 810, 40. doi:10.1088/0004-637X/810/1/40
Dalessandro, E., Ferraro, F. R., Bastian, N., et al. 2019, A&A, 621, A45. doi:10.1051/0004-6361/201834011
Deras, D., Cadelano, M., Ferraro, F. R., et al. 2023, ApJ, 942, 104. doi:10.3847/1538-4357/aca9ce
Deras, D., Cadelano, M., Lanzoni, B., et al. 2024, A&A, 681, A38. doi:10.1051/0004-6361/202347547
Djorgovski, S. 1993, Structure and Dynamics of Globular Clusters, 50, 373
Dresbach, F., Massari, D., Lanzoni, B., et al. 2022, ApJ, 928, 47. doi:10.3847/1538-4357/ac5406
Elson, R. A. W., Fall, S. M., & Freeman, K. C. 1987, ApJ, 323, 54. doi:10.1086/165807
Elson, R. A. W., Freeman, K. C., & Lauer, T. R. 1989, ApJ, 347, L69. doi:10.1086/185610
Elson, R. A. W. 1991, ApJS, 76, 185. doi:10.1086/191568
Ferraro, F. R., Fusi Pecci, F., & Buonanno, R. 1992, MNRAS, 256, 376. doi:10.1093/mnras/256.3.376
Ferraro, F. R., Fusi Pecci, F., Testa, V., et al. 1995, MNRAS, 272, 391. doi:10.1093/mnras/272.2.391
Ferraro, F. R., Paltrinieri, B., Fusi Pecci, F., et al. 1997, A&A, 324, 915. doi:10.48550/arXiv.astro-ph/9703026
Ferraro, F. R., Paltrinieri, B., Fusi Pecci, F., et al. 1998, ApJ, 500, 311. doi:10.1086/305712
Ferraro, F. R., Paltrinieri, B., Rood, R. T., et al. 1999, ApJ, 522, 983. doi:10.1086/307700
Ferraro, F. R., D'Amico, N., Possenti, A., et al. 2001, ApJ, 561, 337. doi:10.1086/322773
Ferraro, F. R., Sills, A., Rood, R. T., et al. 2003a, ApJ, 588, 464. doi:10.1086/374042
Ferraro, F. R., Possenti, A., Sabbi, E., et al. 2003b, ApJ, 596, L211. doi:10.1086/379536
Ferraro, F. R., Origlia, L., Testa, V., et al. 2004, ApJ, 608, 772. doi:10.1086/420837
Ferraro, F. R., Lanzoni, B., Dalessandro, E., et al. 2012, Nature, 492, 393. doi:10.1038/nature11686
Ferraro, F. R., Lanzoni, B., Raso, S., et al. 2018, ApJ, 860, 36. doi:10.3847/1538-4357/aac01c
Ferraro, F. R., Lanzoni, B., Dalessandro, E., et al. 2019, Nature Astronomy, 3, 1149. doi:10.1038/s41550-019-0865-1
Ferraro, F. R., Lanzoni, B., & Dalessandro, E. 2020, Rendiconti Lincei. Scienze Fisiche e Naturali, 31, 19. doi:10.1007/s12210-020-00873-2
Ferraro, F. R., Lanzoni, B., Vesperini, E., et al. 2023, ApJ, 950, 145. doi:10.3847/1538-4357/accd5c
Fiorentino, G., Lanzoni, B., Dalessandro, E., et al. 2014, ApJ, 783, 34. doi:10.1088/0004-637X/783/1/34
Gaia Collaboration, Vallenari, A., Brown, A. G. A., et al. 2022, arXiv:2208.00211. doi:10.48550/arXiv.2208.00211
Giusti, C., Cadelano, M., Ferraro, F. R., et al. 2023, ApJ, 953, 125. doi:10.3847/1538-4357/ace18e
Giusti, C., Cadelano, M., Ferraro, F. R., et al. 2024, arXiv:2402.18389. doi:10.48550/arXiv.2402.18389
Heggie, D. & Hut, P. 2003, The Gravitational Million-Body Problem: A Multidisciplinary Approach to Star Cluster Dynamics, by Douglas Heggie and Piet Hut. Cambridge University Press, 2003, 372 pp.
Hills, J. G. & Day, C. A. 1976, Astrophys. Lett., 17, 87
King, I. R. 1966, AJ, 71, 64. doi:10.1086/109857
Ibata, R., Bellazzini, M., Chapman, S. C., et al. 2009, ApJ, 699, L169. doi:10.1088/0004-637X/699/2/L169
Lanzoni, B., Dalessandro, E., Ferraro, F. R., et al. 2007, ApJ, 668, L139. doi:10.1086/522927
Lanzoni, B., Ferraro, F. R., Alessandrini, E., et al. 2016, ApJ, 833, L29. doi:10.3847/2041-8213/833/2/L29
Lanzoni, B., Ferraro, F. R., Dalessandro, E., et al. 2019, ApJ, 887, 176. doi:10.3847/1538-4357/ab54c2
Lupton, R. 1993, Princeton, N.J.: Princeton University Press, |c1993
Mackey, A. D. & Gilmore, G. F. 2003, MNRAS, 338, 85. doi:10.1046/j.1365-8711.2003.06021.x
Mackey, A. D., Wilkinson, M. I., Davies, M. B., et al. 2008, MNRAS, 386, 65. doi:10.1111/j.1365-2966.2008.13052.x
Maraston, C. 1998, MNRAS, 300, 872. doi:10.1046/j.1365-8711.1998.01947.x
Marigo, P., Girardi, L., Bressan, A., et al. 2017, ApJ, 835, 77. doi:10.3847/1538-4357/835/1/77
Mazzi, A., Girardi, L., Zaggia, S., et al. 2021, MNRAS, 508, 245. doi:10.1093/mnras/stab2399
McCrea, W. H. 1964, MNRAS, 128, 147. doi:10.1093/mnras/128.2.147
Meylan, G. & Heggie, D. C. 1997, A&A Rev., 8, 1. doi:10.1007/s001590050008
Meurer, G. R., Lindler, D. J., Blakeslee, J., et al. 2003, Proc. SPIE, 4854, 507. doi:10.1117/12.460259
Miocchi, P., Lanzoni, B., Ferraro, F. R., et al. 2013, ApJ, 774, 151. doi:10.1088/0004-637X/774/2/151
Montegriffo, P., Ferraro, F. R., Fusi Pecci, F., et al. 1995, MNRAS, 276, 739. doi:10.1093/mnras/276.3.739
Mucciarelli, A., Origlia, L., Ferraro, F. R., et al. 2006, ApJ, 646, 939. doi:10.1086/504969
Mucciarelli, A., Massari, D., Minelli, A., et al. 2021, Nature Astronomy, 5, 1247. doi:10.1038/s41550-021-01493-y
Nayak, P. K., Subramaniam, A., Choudhury, S., et al. 2016, MNRAS, 463, 1446. doi:10.1093/mnras/stw2043
Olsen, K. A. G., Hodge, P. W., Mateo, M., et al. 1998, MNRAS, 300, 665. doi:10.1046/j.1365-8711.1998.01860.x
Olszewski, E. W., Suntzeff, N. B., & Mateo, M. 1996, ARA&A, 34, 511. doi:10.1146/annurev.astro.34.1.511

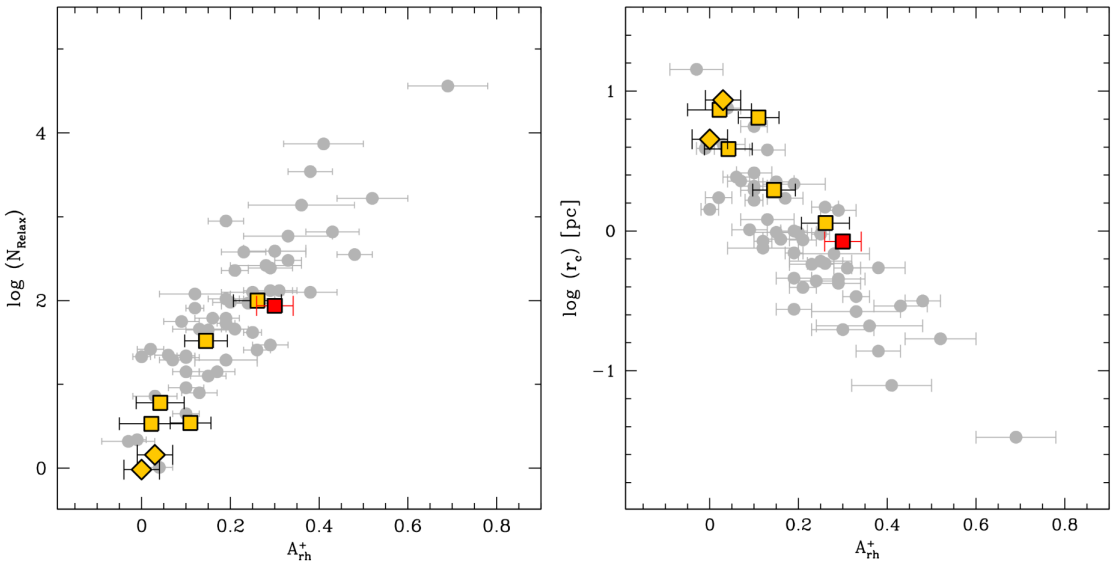

Fig. 7. Final results for NGC 1835 in comparison with other clusters. *Left panel*: Relation between $N_{\rm relax}$ and A^+_{rh} for the star clusters homogeneously investigated so far through the dynamical clock approach: the 52 Galactic GCs discussed in Ferraro et al. (2023) are shown as grey circle, the five LMC clusters discussed in Ferraro et al. (2019) are plotted as yellow squares, the two young star clusters in the SMC discussed in Dresbach et al. (2022) are marked as yellow diamonds, and the determination of NGC 1835 obtained in this work is plotted as a filled red square. *Right panel*: Relation between r_c and A^+_{rh} for the same star clusters plotted in the left panel (same symbols).

Onorato, S., Cadelano, M., Dalessandro, E., et al. 2023, A&A, 677, A8. doi:10.1051/0004-6361/202346792
Pallanca, C., Leanza, S., Ferraro, F. R., et al. 2023, ApJ, 950, 138. doi:10.3847/1538-4357/accce9
Paresce, F., de Marchi, G., & Ferraro, F. R. 1992, Nature, 360, 46. doi:10.1038/360046a0
Pietrzyński, G., Graczyk, D., Gallenne, A., et al. 2019, Nature, 567, 200. doi:10.1038/s41586-019-0999-4
Raso, S., Ferraro, F. R., Dalessandro, E., et al. 2017, ApJ, 839, 64. doi:10.3847/1538-4357/aa6891
Raso, S., Pallanca, C., Ferraro, F. R., et al. 2019, ApJ, 879, 56. doi:10.3847/1538-4357/ab2637
Raso, S., Libralato, M., Bellini, A., et al. 2020, ApJ, 895, 15. doi:10.3847/1538-4357/ab8ae7
Rich, R. M., Shara, M. M., & Zurek, D. 2001, AJ, 122, 842. doi:10.1086/321164
Spitzer, L. 1987, Princeton, N.J. : Princeton University Press, c1987.